

The flow structure in the wake of a fractal fence and the absence of an “inertial regime”

C. J. Keylock · K. Nishimura · M. Nemoto · Y. Ito

Received: 1 July 2011 / Accepted: 15 December 2011
© Springer Science+Business Media B.V. 2012

Abstract Recent theoretical work has highlighted the importance of multi-scale forcing of the flow for altering the nature of turbulence energy transfer and dissipation. In particular, fractal types of forcing have been studied. This is potentially of real significance in environmental fluid mechanics where multi-scale forcing is perhaps more common than the excitation of a specific mode. In this paper we report the first results studying the detail of the wake structure behind fences in a boundary layer where, for a constant porosity, we vary the average spacing of the struts and also introduce fractal fences. As expected, to first order, and in the far-wake region, in particular, the response of the fences is governed by their porosity. However, we show that there are some significant differences in the detail of the turbulent structure between the fractal and non-fractal fences and that these override differences in porosity. In the near wake, the structure of the fence dominates porosity effects and a modified wake interaction length seems to have potential for collapsing the data. With regards to the intermittency of the velocities, the fractal fences behave more similarly to homogeneous, isotropic turbulence. In addition, there is a high amount of dissipation for the fractal fences over scales that, based on the energy spectrum, should be dominated by inter-scale transfers. This latter result is consistent with numerical simulations of flow forced at multiple

C. J. Keylock (✉)
Department of Civil and Structural Engineering, University of Sheffield, Mappin Street,
Sheffield S1 3JD, UK
e-mail: c.keylock@sheffield.ac.uk

K. Nishimura
Graduate School of Environmental Studies, Nagoya University, Furo-cho, Chikusa-ku, Nagoya 464-8601,
Japan

M. Nemoto
Nagaoka Institute for Snow and Ice Studies, Suyoshi, Nagaoka, Niigata 940-0821, Japan

Y. Ito
Nagaoka Institute for Snow and Ice Studies, Shinjo Branch, 1400 Tokamachi, Shinjo, Yamagata
996-0091, Japan

scales and shows that what appears to be an “inertial regime” cannot be as production and dissipation are both high.

Keywords Turbulence · Wakes · Fractal forcing · Intermittency · Inter-scale energy transfer

1 Introduction

Manipulating the characteristics of boundary-layer turbulence is an important area of environmental fluid dynamics engineering as changes to turbulence structure can be used to enhance the deposition of saltating [43] or drifting particles [6, 10], clear runways of drifting snow [33], or influence pollutant dispersal [38]. Understanding how such engineering structures affect turbulence is, consequently, of some importance and the most common type of design used to control the drifting of saltating or suspended particles (usually snow or sand) is a porous fence. The fences must extract sufficient energy from the mean flow to promote deposition, while preventing the development of excessive turbulent stresses that will cause remobilization. The specification for these fences is traditionally in terms of height and an optimal porosity [52], with 50% porosity and a bottom gap of 10% the height of the fence considered optimal for snow drifting [20, 51]. However, experimental results suggest that 50% porosity is not optimal on steep terrain [41] and the inclination of the fence with respect to the wind vector must also be considered [53]. The aim of this paper is to explore a possible further important consideration on the design of such fences: the manner in which the porous elements are organized.

This is not simply a question of practical relevance, but is related directly to recent discussions about the fundamental nature of turbulence, considered in the next section. A turbulent flow forced at some length scale that is much greater than the viscous length scales in the flow, will exhibit an average transfer of energy to smaller scales that can be represented in the Fourier domain as a power-law with a $-5/3$ exponent [26], although the intermittent behaviour of dissipation at small scales means that a multifractal description of turbulence is more correct [13, 27, 39, 40], and even this is not the full story given the range of types of singularity that may occur in a turbulent flow [54]. However, if one manipulates turbulence by forcing it at multiple scales in a controlled manner, what impact does this have on the way in which energy is transferred between scales? It is the investigation of such questions that has recently been of significant experimental and theoretical interest in fluid mechanics and have led to the suggestion that such fractal-forced flows are a new kind of turbulent flow [50]. Hence, it follows that flow through porous fences in boundary layers can potentially make use of such work in order to optimise the design of engineering structures. Thus, such a question merits further experimental investigation.

2 Theoretical context

In a key early analysis, von Karman and Howarth [55] showed how, by assuming a single length and velocity scale, the energy decay for isotropic turbulence would follow a t^{-1} scaling, where t is time. However, early experiments showed that $u^2 \approx t^q$; $q < -1$ [9] and it can be shown that $q = -1$ is a limit state.

The dissipation in homogeneous turbulence is given by

$$\epsilon = 15\nu \left\langle \left[\frac{\partial u}{\partial x} \right]^2 \right\rangle = 15\nu \frac{u^2}{\lambda^2} \tag{1}$$

where λ is the Taylor length scale of the flow by definition and according to von Karman and Howarth [55]:

$$\lambda^2 = -(10/q)\nu t \tag{2}$$

Defining the Taylor Reynolds number as $R_\lambda = u\lambda/\nu$, it follows from (2) and $u^2 \approx t^q$ that

$$R_\lambda \approx t^{(q+1)/2} \tag{3}$$

Hence, as turbulence decays in the absence of an energy input, an upper bound on q is -1 , which is attained at infinite Reynolds number where dissipation is zero. Following George [15] it follows that the shape of the spectrum characterising energy decay is a function of q and, thus, of the initial conditions generating the flow. Furthermore, while von Karman and Howarth [3] and Batchelor [55] make the assumption that the non-linear spectral energy transfer, T_s is proportional to u^3 , the more general result obtained by George [15] is that

$$T_s = \nu(u^2/\lambda) = R_\lambda^{-1}u^3 \tag{4}$$

where $T(k, t)$ is the spectral energy transfer, as a function of time, t , and wavenumber, k , and this is separated into time and wavenumber dependent components as $T(k, t) = T_s(t)g_T(k\lambda, *)$, where $*$ represents a dependence on initial conditions. Note that the Reynolds number dependence in the spectral transfer of energy in this theory means that there is agreement with Kolmogorov’s work at infinite Reynolds number. Hence, Kolmogorov’s expression for the energy spectrum for isotropic values

$$E(k) = \nu^{5/4}\epsilon^{1/4}f_K(kL_K) \tag{5}$$

where L_K is the Kolmogorov length scale, $L_K = \nu^{3/4}/\epsilon^{1/4}$, needs to be re-expressed in terms of Taylor scales:

$$\nu^{5/4}\epsilon^{1/4}f_K(kL_K) = u^2\lambda f_T(k\lambda, *) \tag{6}$$

$$f_K(kL_K) = 15^{-1/4}R_\lambda^{3/2}f_T(k\lambda, *) \tag{7}$$

where f_K is the Kolmogorov spectrum, which is believed to be universal, and f_T is the Taylor-based spectrum that admits a dependence on initial conditions [15]. From (3) it follows that if $q = -1$, R_λ is constant and then from (7) there is a simple proportionality between the two cases. Clearly, at finite Reynolds number this breaks down, which suggests a rescaling of the turbulence spectrum to reflect this. Subsequent numerical calculations using direct numerical simulation (DNS) of the Navier–Stokes equations for decaying turbulence have confirmed these results [56].

George and Wang [16] revisited these solutions with the additional assumption that the length scale for the problem, λ , maintained a constant value. In this case, the whole spectrum and the energy were found to decay exponentially with time with a constant integral and Taylor scale maintained (meaning that their ratio defined the effective Reynolds number of the flow). Hence, the behaviour of the whole spectrum is governed by the Taylor scale, which is a profound result given the traditional emphasis placed on integral and Kolmogorov scales.

Until recently there were no experimental observations to support this argument for exponentially decaying turbulence. However, recent experiments by Vassilicos and co-workers

[19, 35, 47] have shown that in the case of turbulence behind fractal grids, very fast, comparable to exponential, decay is observed. Hurst and Vassilicos [19] studied 21 different fractal grids of various configurations and measured the flow along the centre-line of the wind tunnel. These grids generated higher turbulence intensities and Reynolds numbers than could be achieved for classical grids, even when the latter had lower porosities. It was found that the fractal dimension of the grid, D_f , the effective mesh size of the grid and the ratio of the thickness of the largest and smallest elements in the fence to all be important controls on the turbulence generated. Different types of iterated pattern (I-shape or square grids) exhibited different scalings for the turbulence intensities that were a function of the effective mesh size and thickness ratio. Despite the fact that grids are passive structures, Hurst and Vassilicos suggested that by tuning the properties of the grid, it may be possible to control turbulence intensity, which has important implications for using fractal fences for engineering control.

The work of George and Wang [16] was applied to fractal grids by Mazellier and Vassilicos [35] to explicitly link the observed fast decay to theory. The thickest bars in the fractal grid were used to define a fractal grid Reynolds number, R_{fr} , and then the spectral energy equation

$$\frac{\partial}{\partial t} E(k, t) = T(k, t) - 2\nu k^2 E(k, t) \tag{8}$$

was written in terms of the fractal grid dependencies on the spectral energy transfer and energy spectrum:

$$E(k, t) = E_s(t, U_\infty, R_{fr}, *) f[k, l(t), R_{fr}, *] \tag{9}$$

$$T(k, t) = T_s(t, U_\infty, R_{fr}, *) g[k, l(t), R_{fr}, *] \tag{10}$$

where l is a length scale that in the George and Wang [16] theory exhibits a relation to λ , the dependencies included in $*$ are now those that result from the properties of the fractal grid (dimensionless ratios of the bar lengths and thicknesses that make up the fence), and f and g are dimensionless functions. Criteria for using (9) and (10) to solve (8) were given as

$$\frac{d}{dt} E_s = -a \frac{2\nu}{l^2} E_s \tag{11}$$

$$T_s = b \frac{d}{dt} E_s \tag{12}$$

$$\frac{dl}{dt} = \frac{c \frac{dE_s}{dt}}{E_s} \tag{13}$$

where a , b , and c are functions of $*$ and R_{fr} . The generalisation of the theory of George and Wang [16] by Mazellier and Vassilicos [35] is a consequence of the behaviour of c . When $c = 0$, $d\lambda/dt = 0$ and the George and Wang solution results:

$$E_s(t) \approx \exp\left(-2a \frac{\nu t}{l^2}\right) \tag{14}$$

It follows from this making use of $\frac{3}{2}u^2 = \int_0^\infty E(k, t) dk$ and Taylor's hypothesis that

$$u^2 = u_0^2 \exp\left(-2a \frac{\nu x}{l^2 U_\infty}\right) \tag{15}$$

However, if $c < 0$, Mazellier and Vassilicos [35] showed that a steep power-law applies instead:

$$u'^2 = \frac{2E_s(x_0)}{3l(x_0)} \left[1 + \frac{4\nu a|c|}{l^2(x_0)U_\infty} (x - x_0) \right]^{(1-c)/2c} \tag{16}$$

where the 0 subscript indicates a virtual origin. With this expression the Taylor microscale is given by:

$$\lambda \approx \frac{l(x_0, R_{fr}, *)}{\sqrt{2a(1-c)}} \left[1 + \frac{4\nu a|c|}{l^2(x_0)U_\infty} (x - x_0) \right]^{1/2} \tag{17}$$

Note that as $c \rightarrow 0$ that the Taylor scale becomes independent of $x - x_0$ and that if $\frac{4\nu a|c|}{l^2(x_0)U_\infty} (x - x_0)$ is much less than 1, then (17) permits an increase in λ in the far-field as can be observed in the data of Mazellier and Vassilicos [35]. Irrespective of whether or not the decay in this region is exponential or a steep power-law, the nature of this turbulence is very different to classical flows with the assumed Richardson–Kolmogorov cascade.

In addition to these experimental and theoretical analyses, numerical experiments have been undertaken using Direct Numerical Simulation (DNS) where, instead of forcing the flow at one large wavenumber, a fractal forcing has been adopted, with a range of wavenumbers forced in a power-law fashion [30,31,36,37]. As this modelling progressed from the forcing of some discrete wavenumbers [37], to a continuous forcing it was found that the interscale energy transfer was reduced by a fractal forcing compared to the predictions of Renormalization Group theories. That is, in a region that looked qualitatively like an inertial regime (although more shallow) from the velocity spectrum, significant dissipation ($\approx 80\%$ of the total dissipation) was taking place. That is, a multi-scale forcing altered the manner in which energy transfer took place within the flow [36]. More recent numerical studies [30,31] have confirmed these results and explored additional properties of the flow. In particular, they have noted that the modulation of the energy extends beyond the range of the forced scales and that smaller scale forcings enhance the non-local transfer of energy to smaller scales. This idea is consistent with and help explains the spectral short-cut seen in canopy flows [12]. To help explain these numerical results further, Cheskidov et al. [8] extended previous work deriving bounds on the energy dissipation for simpler forces to the case of broadband and fractal forcings. They obtain a relation between dissipation and Reynolds number consistent with that of Mazzi and Vassilicos [36] and also found that the dissipation for a Stokes flow driven by the same forcing provides the (laminar) upper limit for the dissipation of these turbulent flows.

3 Experimental design and methodology

3.1 Wind tunnel and anemometry

The experiments were performed in the Cryospheric Environment Simulator at the Shinjo branch of the Nagaoka Institute for Snow and Ice Studies over a fixed rough bed (ice coated snow grains) at -10°C . This is a wind tunnel with a square cross section of 1 m^2 and a 14 m working section (Fig. 1). For more information on this experimental facility, see Nemoto and Nishimura [42] and Kosugi et al. [29].

Measurements were recorded at 5 kHz using a Kanomax cross-wire, constant temperature anemometer (model IFA 300 from TSI Inc.) with a 260 kHz response frequency, a length of 1

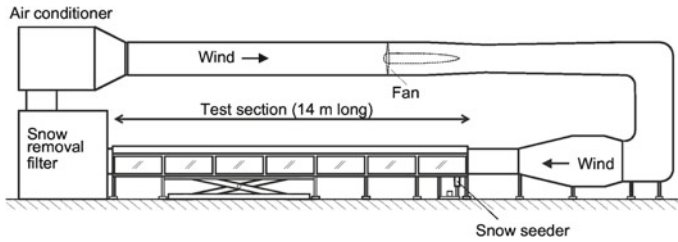


Fig. 1 Side view of the wind tunnel at Shinjo

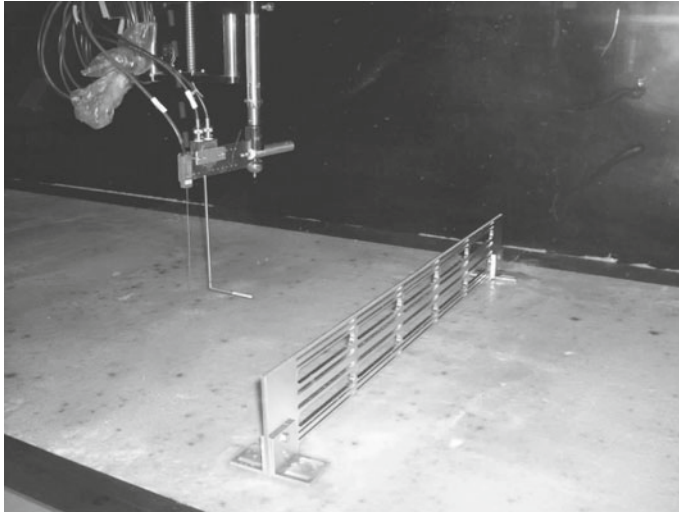


Fig. 2 Measurement of the wake velocity downstream of a fractal fence in the wind tunnel at Shinjo using a hot wire anemometer

mm and a width of $5\ \mu\text{m}$. Calibration of the output voltage was undertaken by relating 3 s of output voltage to an average velocity determined from a sonic anemometer (model DA-650 from Kaijo Sonic in Japan). Signal gain was employed to maximise the $\pm 5\ \text{V}$ output range of the instrument. At 5 kHz, the input noise on the amplifier is $\approx 120\ \text{nV}$.

3.2 Fractal fences

The fences were glued into the tunnel using water and measurements were taken along the centre-line of the wind tunnel (Fig. 2). The simplified fractal nature of the fence is only iterated in the vertical plane, in contrast to a Sierpinski carpet or the fully 2D grids of Hurst and Vassilicos [19] and Seoud and Vassilicos [47], but it does mean that a fractal iterated in this manner interacts with the strong $\partial u/\partial z$ gradient in the flow. In addition, it was only possible to iterate our fractal template three times, meaning that the potential range of scales over which we impose a power-law forcing is reduced compared to previous experiments (e.g. Hurst and Vassilicos [19] used 6 iterations).

In addition to the porosity criterion, snow fences and other passive devices for controlling suspended or saltating particles include a bottom gap of $\approx 0.1H$, where H is the height of the fence, to prevent over-accumulation on the proximal side of the fence [20, 41, 52].

Table 1 Attributes of the fences used in this study

Fence name	Porosity (%)	No. of struts	Mean (standard deviation) of strut spacing (mm)	D_f
5struts50	50	5	10.00 (0.0)	1.000
9struts50	50	9	5.00 (0.0)	1.000
Frac50	50	9	5.00 (4.4)	0.842
Frac60	60	9	6.25 (5.5)	0.774

The spacing calculation excludes the 10 mm bottom gap that is present for all fences

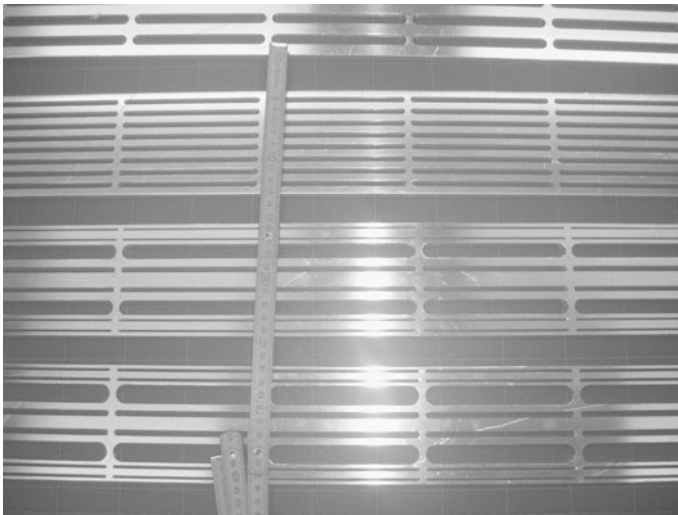


Fig. 3 The fences used in the experiments. From *top to bottom* these are 5struts50 (partially in shot), 9struts50, Frac50 and Frac60

In this study we focus on fences with 50% porosity, but also consider a fractal fence with 60% porosity, where this porosity measure includes a 10 mm bottom gap in all cases but the mean strut spacing does not. Details of the fence specifications are provided in Table 1 and the fences are shown in Fig. 3. Note that our study considers three fences that are indistinguishable based on the standard engineering design criteria but differ significantly in terms of the length scales and range of scales at which they force the flow. All of our fences were $H = 100\text{mm}$ high, 600mm wide, 7mm thick and made from aluminum.

For the 60% fractal fence (Frac60) a reduction in the length scale of a ruler placed vertically on the surface of the fence by a factor of 6 increases the number of rulers covering the fence by a factor of 4 (the fractal is created by dividing a line into 6 parts and deleting the second and fifth part). Hence the linear fractal dimension (D_f) is $\log 4/\log 6 = 0.774$. For the Frac50 fence, which is based on a similar template modified to maintain a lower porosity, $D_f=0.84$. the higher value resulting from the need to maintain a lower porosity.

3.3 Data analysis methods

The data collected using the anemometer were denoised using a now well-known wavelet method [11] with the exception that their cyclical spinning method is replaced by the

stationary or maximal overlap discrete wavelet transform [44], which has the same translation-invariance properties as cyclically rotating the data and is undecimated (if there are $2^J = N$ values in a dataset, where $j = 1, \dots, J$, there will be N detail wavelet coefficients at each scale, j). Hence, it is also a useful tool for surrogate data generation [21, 25]. It is assumed that noise is concentrated preferentially in the highest frequencies (first wavelet scale). A threshold value, T , is then defined based on the variance of the wavelet coefficients and the length of the record assuming Gaussianity (which is not a strong constraint for wavelet coefficients even if the underlying data are non Gaussian):

$$T = \tilde{\sigma} \sqrt{2 \log N} \tag{18}$$

where a robust estimator of $\tilde{\sigma}$ can be found from the fact that the median absolute value, M , of a set of independent zero-mean Gaussian random variables with variance, $\tilde{\sigma}^2$ is $M \approx 0.6745\tilde{\sigma}$. In this paper we use a soft-thresholding algorithm, where the original wavelet detail coefficients, $w_{j,k}$ for all j are modified as:

$$w_{j,k}^* = \begin{cases} w_{j,k} - T & \text{if } w_{j,k} \geq T \\ w_{j,k} + T & \text{if } w_{j,k} \leq -T \\ 0 & \text{if } |w_{j,k}| \leq T \end{cases} \tag{19}$$

where for the remainder of this paper, denoising is presumed to have occurred and the asterisk in (9) is lost. We preceded this denoising with a despiking step based on similar principles but with a much higher value for T [18].

In this paper we use a structure-function based approach for defining the “inertial range” in our experiments and for characterizing the structure of the wake flow. The structure function, S of a given order, n is:

$$S_n(r) = \langle |u_i(x+r) - u_i(x)|^n \rangle \tag{20}$$

and the structure function exponent, ξ_n , is

$$S_n(r) \approx r^{\xi_n} \tag{21}$$

where we use a modified Taylor’s hypothesis (described below) to convert a measured time series into a spatial series.

Energy transfer is conceptualized by equating the third order structure function with $-\frac{4}{5}\epsilon r$, where r is the increment distance and ϵ is the mean dissipation rate [26]. For both higher [1] and lower [7] order structure functions the scaling relations depart from those predicted by Kolmogorov (who found $\xi_n = \frac{n}{3}$), owing to intermittency. For example, the model of She and Leveque [48] gives

$$\xi_n = \frac{n}{9} + 2 \left[1 - \left(\frac{2}{3} \right)^{\frac{n}{3}} \right] \tag{22}$$

for three-dimensional, homogeneous turbulence. More recently, it has been shown that the values for the scaling exponents can vary spatially in wake flows [14].

We used the Extended Self-Similarity (ESS) of Benzi et al. [4] to obtain an improved estimate of the velocity structure function scaling exponents than is possible from the direct analysis of S_n against r . This method extracts the exponents (for all n except 3) from a plot of exponent $S_n(r)$ against $S_3(r)$ and works because the ratio of two scaling exponents is constant over a greater range of scales than is the case when each is examined individually. This scaling has been found to hold to within an order of magnitude of η and not just within the inertial regime [5] and the resulting relative scaling exponents also hold for 2D flow [2].

Because the flow that we are studying is highly turbulent, a simple Taylor’s hypothesis does not hold [34]. However, this conversion can still be undertaken with an appropriate definition of the local average velocity. The method we adopted is due to Pinton and Labbé [45] and uses an integral time scale, I , defined as a function of the energy spectrum $E(f)$:

$$I = \frac{\int E(f)df}{\int f E(f)df} \tag{23}$$

where f is frequency. Using I it is possible to obtain a local average velocity as a function of time

$$\bar{u}_{loc}(t) = \frac{1}{T} \int_{t-I/2}^{t+I/2} u(\hat{t})d\hat{t} \tag{24}$$

Thus, the point in space x for a measurement made at time t^* is

$$x = \int_0^{t^*} \bar{u}_{loc}(t)dt \tag{25}$$

which is then resampled onto regular increments. As well as applying this procedure before deriving spectra as a function of inverse space rather than inverse time, we also adopted an alternative technique due to Gledzer [17] who found that the true spectrum E_{real} could be obtained from the measured version E_{meas} according to

$$E_{real}(k) = \left[1 - \frac{1}{2} \left(\frac{u'}{U} \right)^2 \left(\frac{22}{9} + \frac{10}{3} \beta k \eta + (\beta k \eta)^2 \right) \right] E_{meas}(k) \tag{26}$$

where k is wavenumber and U and u' are the mean and fluctuating velocities from a Reynolds decomposition. It was found by Saddoughi and Veeravali [46] that $\beta \approx 5.3$ and this is compatible with that measured for wakes from fractal objects [49]. In Eq. 26, the Kolmogorov length scale η was evaluated as $\eta = (\nu^3/\epsilon)^{\frac{1}{4}}$, where ν is the kinematic viscosity and the dissipation, ϵ , is given by

$$\epsilon = 2\nu \int k^2 E(k)dk \tag{27}$$

4 Results

4.1 Mean flow properties

The results reported in this paper are for a mean flow velocity in the tunnel of 6 m s^{-1} . With the 1 m height of the tunnel, this gives a flow Reynolds number of $Re \approx 467000$. The median Taylor Reynolds number, $Re_\lambda, 10H$ before the fence at $z/H = 0.55$ over all experiments was 193, which was estimated from (1), with the velocity derivative defined over the inertial range, which was, in turn, estimated from the region of a log–log plot of S_3 against r where the slope was 1.0.

The mean velocity profiles as a function of height above the boundary, $U_1(z)$, upstream of the fence (at $-10x/H$) are shown in Fig. 4a, plotted in wall units. Profiles downstream of the

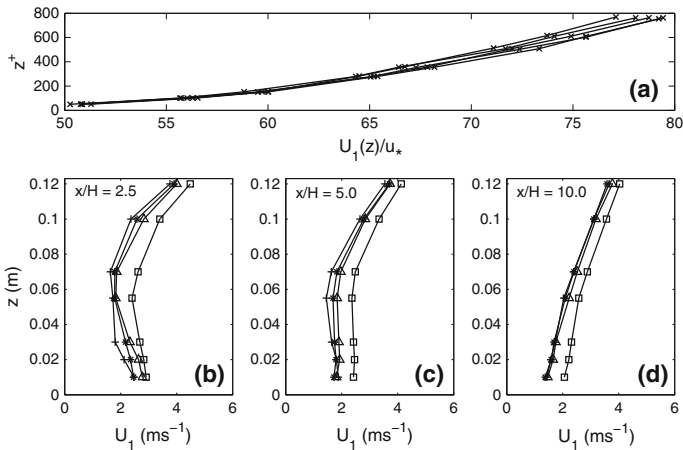


Fig. 4 Profiles of the mean longitudinal velocity, U_1 , as a function of distance from the wall, z . **a** The *top panel* is for data upstream of the fence and is plotted in wall units where z is non-dimensionalised by the kinematic viscosity and the friction velocity. The *other panels* are dimensional and show vertical profiles at $x/H = 2.5$ (**b**), $x/H = 5.0$ (**c**), and $x/H = 10.0$ (**d**). Symbols correspond to: * (5struts50), + (9struts50), Δ (Frac50), \square (Frac60)

fence are shown in the other panels. There is a good collapse of the data at $-10x/H$, particularly for $z < 0.10\text{m}$ (the height of the fence), which corresponds to $z^+ \approx 600$. Downstream of the fence, porosity dictates behaviour, with similar profiles for the three fences with 50% porosity, particularly at $x/H = 10.0$. By this point the profile is beginning to recover from the velocity defect that is clearly in evidence closer to the fence. The higher velocities for the Frac60 fence indicate that the 50% porosity is more effective at extracting energy from the mean flow, as is well-known. Hence, in terms of mean flow, there would appear to be no strong effect of multi-scale forcing.

4.2 Turbulence intensity

Figure 5a shows the values for the root-mean-square velocity, $\sigma(u_1)$, at a height of $z/H = 0.55$ along the centre-line of the wind tunnel for varying x/H normalized by the mean velocity at each of these locations. The bottom gap of 10 mm and total fence height of 100 mm means that $z/H = 0.55$ is at the centre of the region of the fence occupied by horizontal struts. The high turbulence intensities close to the fence and the rapid decay downstream are clearly visible in the fractal case and are patterns that have been seen in previous work [49]. For $x/H \geq 5.0$, the three fences with 50% porosity exhibit very similar turbulence intensities, while the more porous fractal fence exhibits a marked reduction. Figure 5b normalizes $\sigma(u_1)$ by the mean velocity at $z/H = 0.55$ for a position upstream of the fence ($x/H = -10$), which varied from 4.135 to 4.199 ms^{-1} over the four experiments. The totally different behaviour of the more porous, Frac60 fence is clear here. The greater turbulence intensity of the fractal fence, Frac50, particularly when compared to 9struts50, which has the same porosity and average scale of forcing, is also evident. This indicates that there is an effect from multi-scale forcing on the turbulence intensity near the fence.

Figure 6 supports the conclusion that the effect of a fractal configuration upon turbulence intensity is predominantly within $x/H < 5.0$. In Fig. 5a the two fractal fences have a vertical profile for $\sigma(u_1)$ that is similar in form, with the values for Frac60 approximately the same as

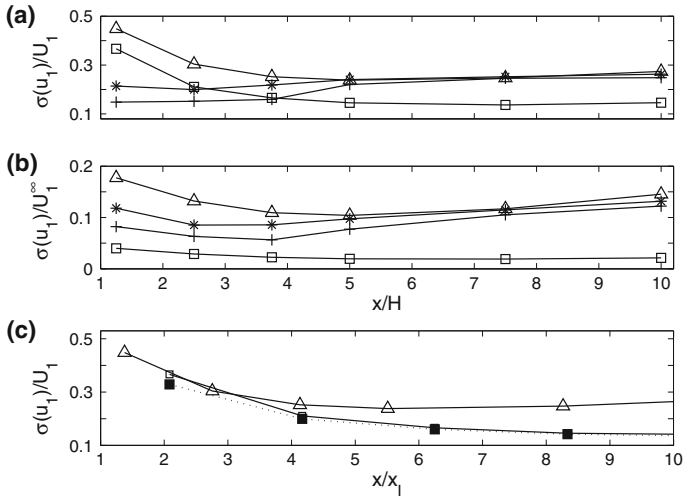


Fig. 5 The turbulence intensity, $\sigma(u_1)$ for the longitudinal velocity component at $z/H = 0.55$. Symbols correspond to: * (5struts50), + (9struts50), Δ (Frac50), \square (Frac60). In **a**, $\sigma(u_1)$ is normalized by the mean, local longitudinal velocity U_1 , while in **b** it is normalized by the mean velocity at $z/H = 0.55$ upstream of the fence (U_1^∞). In **c**, the data from 5a are scaled by the eddy interaction length, x_l as described in the text. The \blacksquare symbol with a dotted line shows the results for the Frac60 fence at a higher reference velocity of 8 m s^{-1}

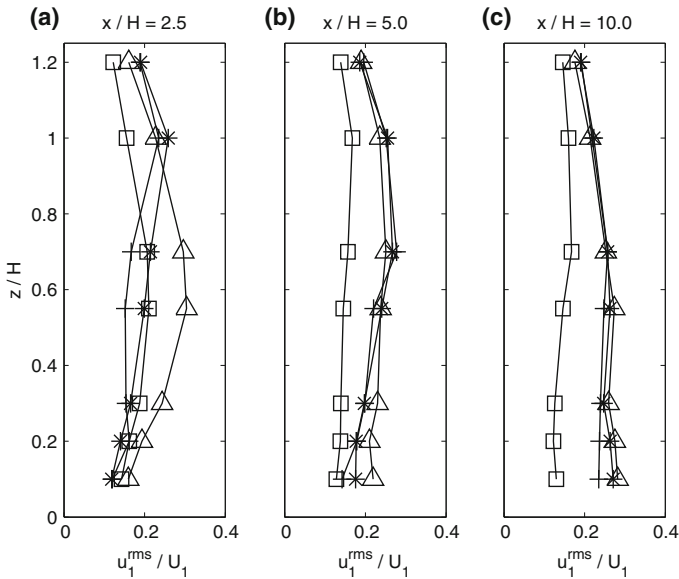


Fig. 6 Vertical profiles of $\sigma(u_1)$ at $x/H = 2.5$ (**a**), $x/H = 5.0$ (**b**), and $x/H = 10.0$ (**c**). Symbols correspond to: * (5struts50), + (9struts50), Δ (Frac50), \square (Frac60)

for the non-fractal fences and the values for Frac50 somewhat higher. The reduced turbulence intensity for the fractal fences at the top of the fence is probably explained by weaker shearing due to locally greater porosity. (For 5struts50 and 9struts50, the closest gap in the fence is 10 mm or 5.5 mm from the top, respectively, while this is 3 mm or 2.5 mm for the fractal

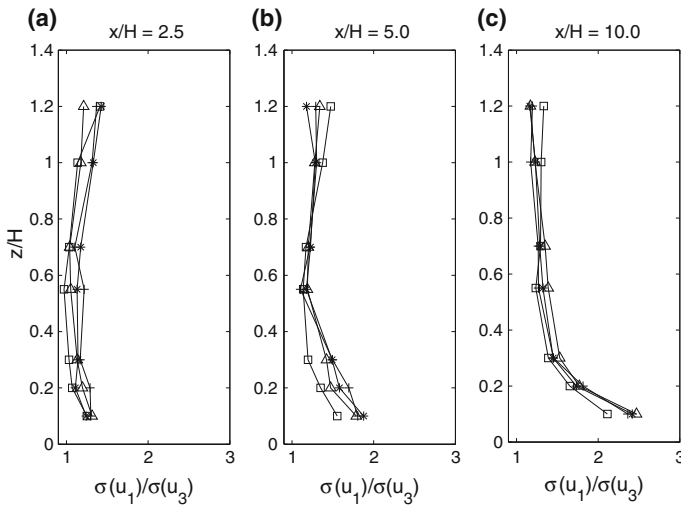


Fig. 7 Profiles of the turbulence anisotropy at locations $x/H = 2.5$ (a), $x/H = 5.0$ (b), and $x/H = 10.0$ (c). The symbols are the same as in Fig. 5

fences). For $x/H \geq 5.0$ all the profiles become relatively uniform and the varying porosity between Frac60 and the other fences is the explanation of the observed differences, with a convergence in behaviour for $z = 0.12$ m, where the direct effect of the forcing is reduced.

Mazellier and Vassilicos [35] introduced an eddy-interaction length scale, x_I , on the basis that typical wake widths will scale with the size of the generating strut in the fence, and that wakes from smaller bars will merge and interact closer to the fence, such that the largest strut in the fence controls the wake-merger distance. It was observed that the distance downstream to the peak in streamwise turbulence intensity was $0.45x_I$. Figure 6 indicates that $x_I < 5H$ for all our fences because at this distance, porosity effects dominate behaviour and the vertical profiles have homogenised. Hence, such a scaling should only be of use for the first three measurements, at most. Because our arrangement of struts was denser than that used by Mazellier and Vassilicos [35], we found that we obtained better results based on the maximum spacing between struts rather than the size of the strut. Hence, our definition of the wake interaction length, x_I , is $x_I = z_d^2/z_m$, where z_d is the vertical separation between the largest gaps in the fence and z_m is the maximum size of spacing between struts. Figure 5c applies such a scaling to the data in 5a and would appear to have some relevance for scaling the turbulence intensity near the fence. In order to add some additional confidence to this result, Fig. 5c also shows results for the Frac60 fence with a mean flow velocity in the wind tunnel of 8 m s^{-1} rather than 6 m s^{-1} , and it follows a similar collapse in the near-wake region. In conclusion, it would appear that while porosity is the dominant control on far-wake turbulence intensity, in the near-wake the fractal nature of the fence exerts an important effect. A modified wake interaction length scale seems to have some potential for collapsing these data.

4.3 Isotropy and increment distributions

In order for statements about velocity component u_1 to generalise to describing the flow at a point, the flow should be approximately isotropic. A simple measure of anisotropy is the ratio $\sigma(u_1)/\sigma(u_3)$, which is given in Fig. 7. While shearing along the bottom gap is enough

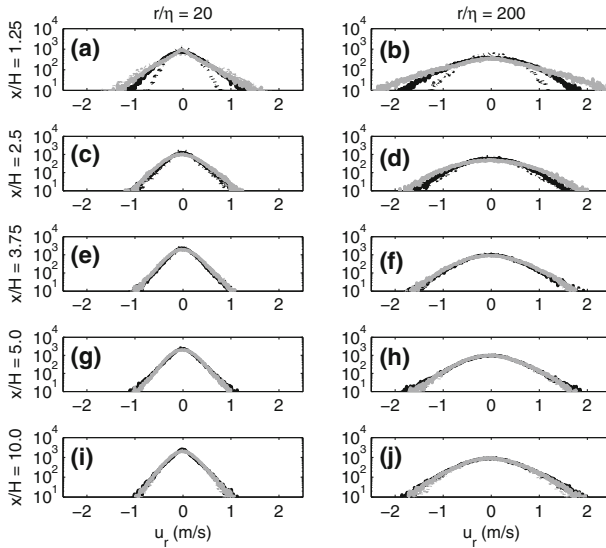


Fig. 8 Longitudinal velocity increment distributions at $z/H = 0.55$ at various locations downstream of the fences and for two values of r/η . The grey dotted line is Frac60, the grey solid line Frac50, the black dotted line is 9struts50 and the solid black line is 5struts50

to result in significant anisotropy close to the bed, higher into the flow, the isotropy is not unreasonable, particularly at $z/H = 0.55$ where most of our analysed data are from.

Figure 8 shows the velocity increment distributions $u_r = u_1(x + r) - u_1(x)$ at various x/H for $z/H = 0.55$. Results are shown for $r/\eta = 20$ (left panels) and $r/\eta = 200$ (right). The fractal fences have the heavier tailed distributions close to the fence and they are difficult to distinguish from one another despite their difference in porosity. However, for $x/H \geq 3.75$ the four fences are practically indistinguishable. The difference between the fractal and non-fractal fences also occurs close to the fence at $z/H = 0.10$ (Fig. 9) and is very clear, with the black and grey lines clearly distinct (although the 2 lines of the same colour are virtually indistinguishable from one another). Although Fig. 7 shows that results from $z/H = 0.1$ need to be interpreted with caution, Figs. 8 and 9 in combination suggest that there is a genuine difference between the fractal and non-fractal fences close to the fence. The higher kurtosis of the wake for the non-fractal fences indicates differences in the intermittency of the turbulence between the two types of fence, which is a result that is examined in greater detail in the subsequent sections of this paper.

4.4 Roughness of the velocity signals

Further analysis was undertaken to see if the nature of the forcing did leave a more subtle imprint on the flow for $x/H \geq 5.0$. Thus, with reference to Fig. 5, we are sufficiently far from the fence that porosity effects dominate the turbulence intensity and it might be considered that the nature of the forcing from the fence is no longer important. A qualitative assessment of 3.277 s of the wake time series (about 50 integral times) from 9struts50 and Frac50 is given in Figs. 10 and 11 at $(x/H = 5.0, z/H = 0.55)$. These plots use the visualization routines of Keylock [22] and show the flow quadrant events exceeding a hole size threshold, $H_T = 1$, given by:

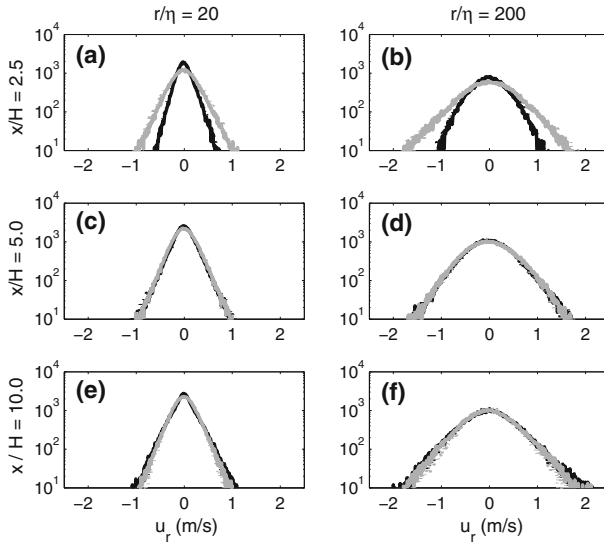


Fig. 9 Longitudinal velocity increment distributions at $z/H = 0.10$ at various locations downstream of the fences and for two values of r/η . The fences are distinguished using the same line types as in Fig. 8

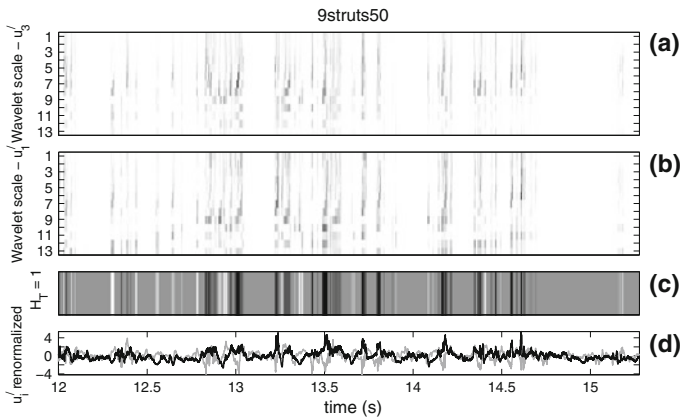


Fig. 10 Qualitative analysis of quadrant flow structures for 3.28 s of data at $(x/H = 5.0, z/H = 0.55)$ for the 9struts50 fence

$$|u'_1 u'_3| > H_T \sigma(u'_1) \sigma(u'_3) \tag{28}$$

where the subscripts 1 and 3 refer to the longitudinal and vertical velocity components and the prime indicates a fluctuating velocity. The time series for the u'_i are shown in Figs. 10d and 11d, normalized by their standard deviations. The threshold exceedances are given in 10c and 11c, with black indicating a sweep ($u'_1 > 0, u'_3 < 0$), white an ejection ($u'_1 < 0, u'_3 > 0$), dark grey an outward interaction ($u'_1 > 0, u'_3 > 0$) and light grey and inward interaction ($u'_1 < 0, u'_3 < 0$). The remaining two plots in each figure show a stationary wavelet decomposition of each velocity component with shading proportional to the value of the wavelet coefficients $w_{j,k}$, if the coefficients are contributing to the highlighted event (i.e. they have the same sign as the flow feature at the point in time). The shading is normalized on a

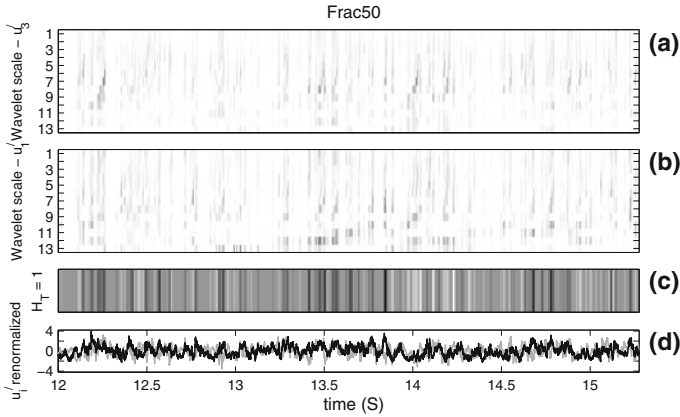


Fig. 11 Qualitative analysis of quadrant flow structures for 3.28 s of data at $(x/H = 5.0, z/H = 0.55)$ for the Frac50 fence

scale-by-scale basis over both velocity components so that the wavelet energy at a given scale, k may be compared between velocity components.

Something that is readily apparent from these plots is that threshold exceedances for 9struts50 occur in clusters, while for Frac50 there is a tendency to produce more and shorter exceedances. This suggests that the mean roughness of the Frac50 signal is greater but that the standard deviation of the roughness is higher for 9struts50 (periods of relative quiescence and times when the threshold is exceeded). To test this hypothesis we calculated the pointwise Hölder regularity (α_p) of the signals in Figs. 10 and 11 using an oscillation-based method implemented in the FracLab toolbox (<http://www2.irccyn.ec-nantes.fr/FracLab/>). This measure is discussed in some detail by Kolwankar and Lévy Véhel [28] and has been applied to the analysis of turbulence signals by Keylock [23,24]. The value for α_p at some position along the signal, t_0 , is given by the supremum for s occurring in the set $C_p^s(t_0)$, where a particular segment of stationary velocity data $u(t)$ is a member of this set if there is a polynomial P of degree less than s (where $s > 0$) and a constant, C , such that the following inequality holds:

$$|u(t) - P(t - t_0)| \leq C|t - t_0|^s \tag{29}$$

Hence, the actual signal is compared to its smoothness in terms of its order of differentiability and the exponent α_p can therefore be thought of as a fractal dimension local to a particular point in the time series. Our hypotheses about the signals are borne out in Fig. 12 where $\bar{\alpha}_p$ for 9struts50 is 0.515 and for Frac50 is 0.444 (a lower value is less differentiable and consequently indicates a rougher signal). In addition, both the largest and smallest values for α_p occur for 9struts50, where $\sigma(\alpha_p)$ is 0.059 as opposed to 0.037 for Frac50. Results for the fences at $(x/H = 5.0, z/H = 0.55)$ and $(x/H = 10.0, z/H = 0.55)$ are given in Table 2. The greater average roughness in the fractal-forced cases is in agreement with the DNS results of Mazzi and Vassilicos [36] (see their Fig. 7). Thus, while our earlier analyses suggest that from $x/H = 5.0$ there are no differences in the wake structure of fences with a similar porosity, an analysis using Hölder exponents demonstrates that the wake flow is experiencing a different forcing at such locations, although this is not evident from the velocity and turbulence intensity data.

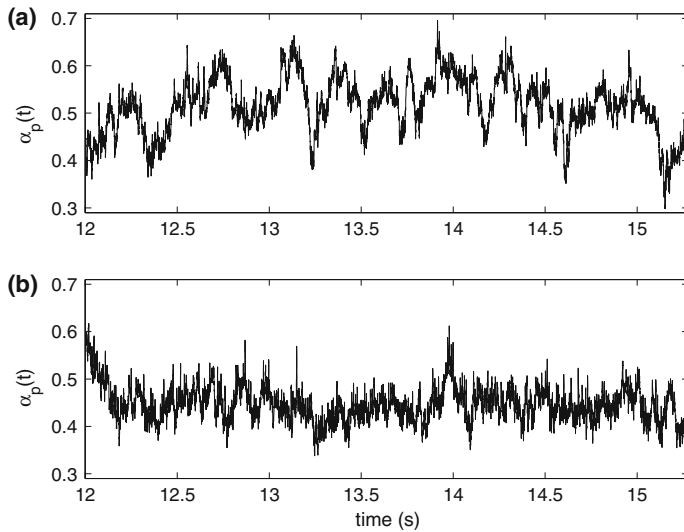


Fig. 12 Time-series of estimated α_p values for the 9struts50 (a) and Frac50 (b) fences studied in Figs. 10 and 11

Table 2 Mean and standard deviations for $\alpha_p(t)$ at ($x/H = 5, z/H = 0.55$) indicated by a¹ superscript and ($x/H = 10, z/H = 0.55$) indicated by a² superscript

Fence name	$\bar{\alpha}_p^1$	$\sigma(\alpha_p)^1$	$\bar{\alpha}_p^2$	$\sigma(\alpha_p)^2$
5struts50	0.496	0.053	0.626	0.083
9struts50	0.515	0.059	0.512	0.055
Frac50	0.444	0.037	0.504	0.047
Frac60 60	0.392	0.033	0.426	0.036

The reduced intermittency for the fractal-forced flows at $x/H \geq 5$ as seen in Table 2 and the figures in this section has implications for sediment transport and deposition. For larger particles, where the small-scale structures seen in Fig. 11 have a negligible effect on entrainment or distraintment, deposition behind fractal fences should be more efficient than for non-fractal fences where fluctuations are more prolonged and may impart greater inertia. Conversely, for smaller particles, fractal fences are expected to be less efficient as the high frequency variations that these wakes exhibit will promote remobilisation and suspension.

4.5 Energy spectra of the velocity signals

Figure 13 shows example energy spectra for u_1 in the wake of the different fences at ($x/H = 3.75, z/H = 0.55$) produced using the multi-taper method and corrected using Eq. 26. The range of values on the x-axis covers a wavenumber that corresponds to the height of the fence, $k = 10 \text{ m}^{-1}$, and all the length scales forced by the gaps in the fences down to $k \approx 5 \times 10^2 \text{ m}^{-1}$, from where the spectra drop away rapidly due to high dissipation. There is a power-law decay region that initiates from the fence height wave number and, from a comparison to the green lines, it is evident that the fractal fences exhibit an energy decay in this region that is closer to $-5/3$ than for the non-fractal fences. Energy decay then appears to be more rapid for the non-fractal fences as indicated by their steeper gradients, although the wavenumber at which this final decay is initiated is dictated by porosity.

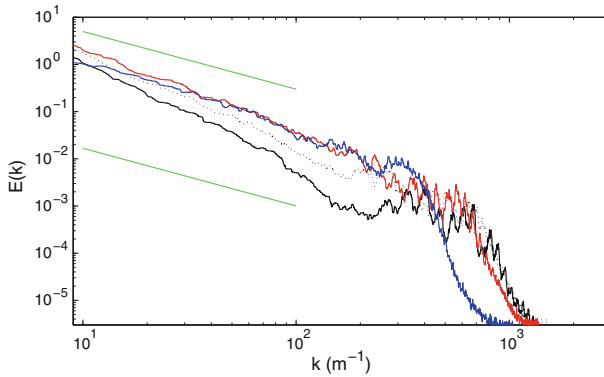


Fig. 13 Energy spectra for the longitudinal velocity component at $(x/H = 3.75, z/H = 0.55)$. The spectra are presented in dimensional form, with *coloured lines* for the fractal fences (Frac50 = red; Frac60 = blue) and *black lines* for the other fences (9struts50 = solid; 5struts50 = dotted). The green lines indicate a $-5/3$ slope

A comparison of these experimental results to recent direct numerical simulations of flow from fractal grids [32] is interesting, although the energy spectra studied by these authors were obtained upstream of the peak in turbulence intensity and, thus, in the production region. In our case, Fig. 5b shows that for the fractal grids we are downstream of the peak, while for the regular grids, $x/H = 3.75$ is a minimum for the turbulence intensity. The data from Laizet and Vassilicos [32] show that at the furthest distance downstream, a $-5/3$ slope is developed over a greater range of scales for fractal-forced flows than for those generated by regular grids, which is in agreement with the results in Fig. 13, although no firm conclusions can be drawn from this comparison given the difference between the two experiments.

In order to study this result in greater detail, the energy spectrum generated at each location for each fence was normalized by its energy peak, E_{max} and a threshold of $0.55 E(k)/E_{max}$ was used to define a low wavenumber location k_{thresh} that was within the energy decay region for all sites. A straight line was then fitted to the log-log plot of $E(k)/E_{max}$ and k for $k_{thresh} \leq k < 20k_{thresh}$, where the upper threshold was determined as an appropriate lower limit of the scaling region over all spectra. The slopes for the fractal fences are generally more shallow than for the non-fractal fences, with those for Frac50 lying closest to $-5/3$ (mean of -1.673), while the Frac60 slopes are the least steep (mean of -1.424). The mean values for 9struts50 and 5struts50 are closer together at -2.005 and -1.949 , respectively. The results for the fractal fences are also less variable, with standard deviations of 0.085 and 0.094 for Frac50 and Frac60, respectively, as opposed to 0.200 for 5struts50 and 0.261 for 9struts50. Hence, the spectra for Frac50 are closest to what would be expected for homogeneous, isotropic turbulence, although this spectrum is developed over a range of scales that are forced by the fence (rather than representing the decay from a large scale forced mode) and we might expect it to consequently, exhibit rather different properties [36].

4.6 Dissipation analysis

The flow is forced by the fence at scales between the fence height ($k \approx 10^1 \text{m}^{-1}$) and the diameter of the smallest strut within the fence. Clearly, the fractal fences will force the flow over a greater range of scales (as they have the smallest strut sizes). However, for 9struts50 and Frac50, the average scale of the forcing is the same. Denoting the fence scale wave

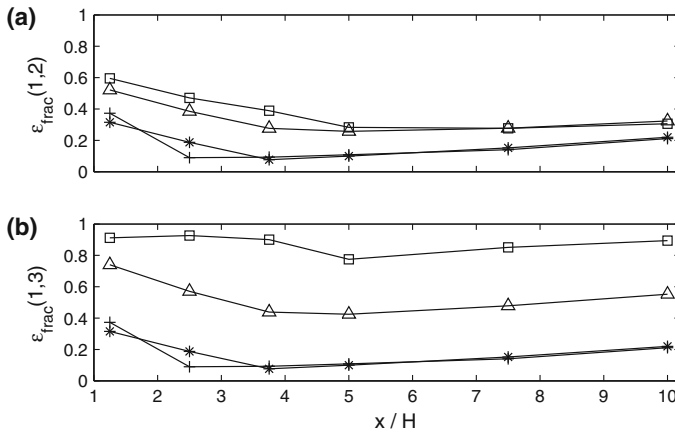


Fig. 14 Values for $\epsilon_{\text{frac}}(1, 2)$ (a) and $\epsilon_{\text{frac}}(1, 3)$ (b) at a height of $z/H = 0.55$ and varying x/H . The symbols used are the same as in Fig. 5

number by k^{*1} , the wavenumber corresponding to the average forced scale as k^{*2} , and the minimum forced scale by k^{*3} , then using Eq. 27, the fraction of dissipation occurring over the forced scales is

$$\epsilon_{\text{frac}}(i, j) = \frac{\int_{k^{*i}}^{k^{*j}} k^2 E(k) dk}{\int_0^\infty k^2 E(k) dk} \tag{30}$$

This term is similar to that used by Mazzi and Vassilicos [36] to analyse the amount of dissipation taking place over the forced scales in their numerical simulations. Values for $\epsilon_{\text{frac}}(i, j)$ at $z/H = 0.55$ are plotted in Fig. 14. Over the range of forced scales there is higher dissipation for the fractal fences and this is particularly the case when the full range of scales forced by the fractal fences is accounted for in Fig. 14b. Note that the wavenumber of the average forcing for 9struts50 is twice that of 5struts50, but $\epsilon_{\text{frac}}(1, 2)$ is very similar at each location. The value for k^{*2} is the same for Frac50 and 9struts50, yet there is a clear difference in their behaviour. It is quite remarkable how the two fractal fences have a very similar behaviour in Fig. 14a despite their difference in porosity, while the two non-fractal fences exhibit much reduced, but virtually identical dissipation too. This suggests that the fractal fences have a genuinely different behaviour in terms of dissipation, although we assume that the wavenumbers derived from the geometry have the same physical control on the local properties of the wake such that there is no additional k dependence behind these results.

Vertical profiles of $\epsilon_{\text{frac}}(1, 2)$ for 9struts50 and Frac50 are shown in Fig. 15. The fractal fence has the higher dissipation in all cases, although there is convergence as x/H and z/H increase. The degree of difference between these two fences is much greater than that for $\sigma u_1/U_1$ in Fig. 5. Hence, the enhanced dissipation at all positions is largely due to the fractal nature of the object and is not an artefact of higher values for turbulence intensity. This is consistent with the work of Mazzi and Vassilicos [36], who explained the effects of fractal forcing with reference to the energy transfer relation:

$$\Phi(k) + I(k) = 2\nu k^2 E(k) \tag{31}$$

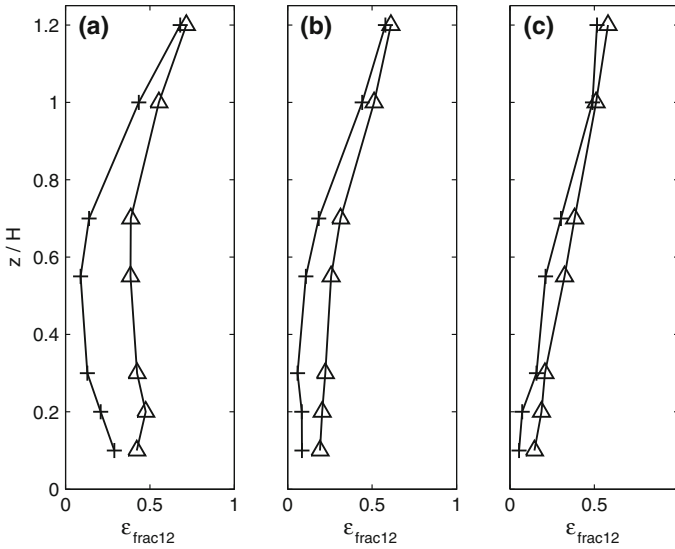


Fig. 15 Values for $\epsilon_{\text{frac}}(1, 2)$ as a function of z/H at $x/H = 2.5$ (a), $x/H = 5.0$ (b) and $x/H = 10.0$ (c). The triangles are Frac50 and the crosses are 9struts50

where $\Phi(k)$ is the energy input spectrum and $I(k)$ is the inter-scale energy transfer. In the fractal-forcing range it was found that $I(k)$ was small, which is the case for very high Reynolds number, equilibrium turbulence. Hence, what seems to be an inertial range for the spectra of the fractal fences in Fig. 13 appears to be a realization of the high dissipation, low $I(k)$ phenomenon described by Mazzi and Vassilicos [36], although the actual amount of dissipation that occurs over this region of the spectrum in the numerical experiments was much higher than observed here. The reduced rate of decay of energy in the spectra for the fractal fences, coupled to the higher dissipation means that significant turbulent production is occurring over the region of log–log energy decay, again indicating that the “inertial regime” label is inappropriate for these wakes. The implication of this is that a more detailed consideration of the factors affecting the relaxation time (usually a settling velocity-based expression) and, thus, the deposition of particles in the wake of fences is needed. A $-5/3$ slope but significant dissipation implies a different turbulence environment where particles may be entrained by strong local dissipation. This raises the possibility of optimising the depositional state by careful control of the nature of the forcing.

4.7 Structure function analysis

When evaluating the exponents using ESS we adopted a lower limit of 20η and an upper limit of $0.75I$, where the integral length scale, I is derived by applying the Pinton and Labbé [45] modified Taylor’s hypothesis to Eq. 13 as described in Sect. 3.3. Equation 20 was used to calculate the structure functions with exponents for $n = 2, 4$ using ESS denoted by $\xi_{2|3}$ and $\xi_{4|3}$, respectively, in this study.

Because the integral length scale is reduced for fractal-forced turbulence due to the smaller scale roughness of the signal (Fig. 12), there were three locations where the difference between $20r/\eta$ and $0.75I$ was insufficient to produce enough samples for $\xi_{2|3}$ and $\xi_{4|3}$ to be evaluated with confidence. Figures 16 and 17 show box and whisker plots for the range of val-

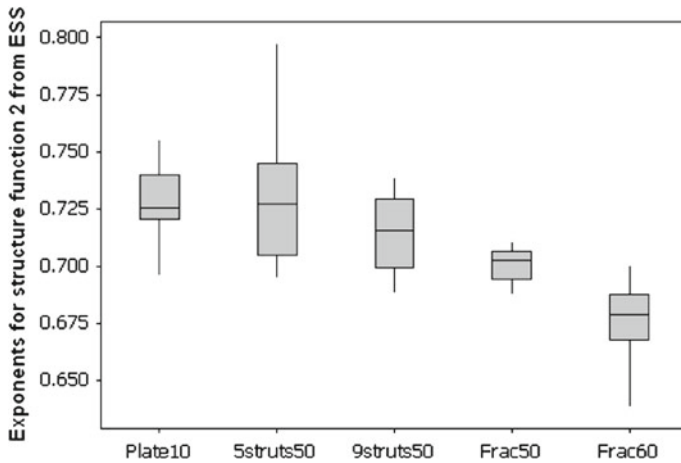


Fig. 16 Box and whisker plots indicating the median (centre line), interquartile range (box) and $Q3 + 1.5(Q3 - Q1)$, $Q1 - 1.5(Q3 - Q1)$ (whiskers) for the values of $\xi_{2|3}$ determined over the sampled region, where $Q1$ and $Q3$ are the first and third quartiles, respectively

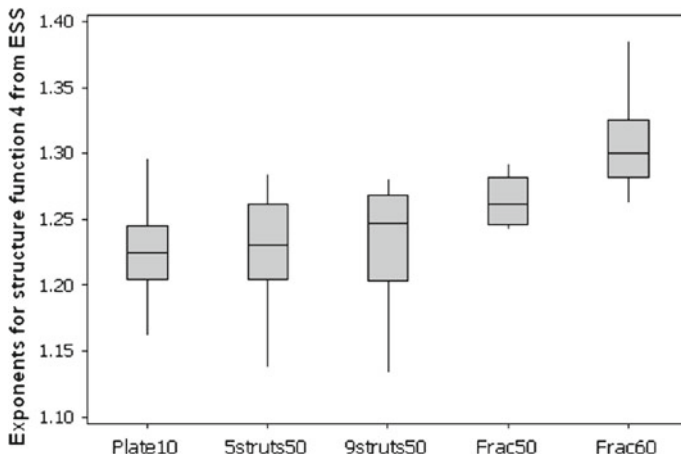


Fig. 17 Box and whisker plots indicating the median (centre line), interquartile range (box) and $Q3 + 1.5(Q3 - Q1)$, $Q1 - 1.5(Q3 - Q1)$ (whiskers) for the values of $\xi_{4|3}$ determined over the sampled region, where $Q1$ and $Q3$ are the first and third quartiles, respectively

ues of $\xi_{2|3}$ and $\xi_{4|3}$ found in the wake of each fence excluding these three sites. Non-parametric statistical tests for the difference in medians found no significant difference between Plate10 (a solid plate with a 10 mm bottom gap), 5struts50 and 9struts50 for either $\xi_{2|3}$ or $\xi_{4|3}$ despite their large differences in porosity. However, statistically significant differences at the 5% level existed between these fences and the two fractal fences, which were in turn different to one another. Figure 18 shows the mean values for $\xi_{n|3}$, $n \in \{2, 4, 6\}$ in the wake region for the five fences compared to values expected from Kolmogorov [26] and She and Leveque [48]. There is a clear tendency for the exponents from the fractal fences to be closer to those predicted for homogeneous turbulence, which suggests that the lower degree of intermittency seen in Fig. 12 for the fractal fences is more akin to that expected for homogenous flow, and is

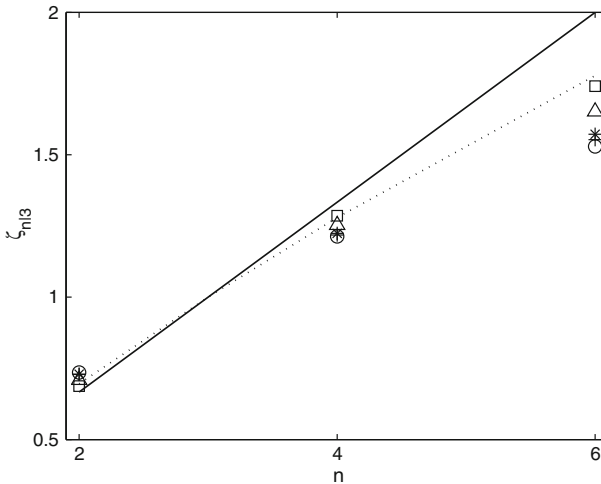


Fig. 18 Mean values for $\xi_{n|3}$ in the wakes for the five fences. The Kolmogorov [26] theory is shown by a *solid line* and that due to She and Leveque [48] is indicated by a *dotted line*. Symbols correspond to: * (5struts50), + (9struts50), Δ (Frac50), \square (Frac60)

consistent with the slopes of the spectra for Frac50 in particular. Usually, exponents that are closer to those predicted from Kolmogorov theory would arise at higher Reynolds number. From Fig. 4 the Reynolds number (based on external scales) is greater than for the other fences and this may explain the result for this fence, although it does not account for the fact that Frac50 exhibits a significantly different response to the other fences with the same porosity and Reynolds number. This implies that not all of the departure of the Frac60 exponents from those for the regular fences can be due to Reynolds number.

In summary, although the turbulence intensities are similar for the wakes of fractal and non-fractal forced fences when normalized by their own local mean velocities for $x/H \geq 5$ (Fig. 5a), the detailed nature of the turbulence structure is quite different between these cases. Thus, a multi-scale fractal forcing leads to differences in the detailed turbulence structure compared to fences with the same porosity but uniform spacing of fence elements. That fractal fences appear to have a multifractal structure and, thus, intermittency that is more akin to homogeneous, isotropic turbulence is potentially useful for developing models for fence behaviour as it implies that theories derived for the homogenous case (such as the log-Poisson model of She and Leveque [48] plotted in Fig. 18) are more applicable to fractal-wake flows than traditional forcings.

5 Conclusion

Previous work reported that fractal objects introduce high turbulence intensities in the near-wake that decay rapidly downstream, and this property is also evident with our relatively simple fractal fences, although differences in porosity dominate over the fractal or non-fractal nature of the fence for $x/H > 5.0$. However, in the near-wake clear differences exist in the longitudinal turbulence intensity, $\sigma(u_1)/U_1$, and it was found that a modified version of the Mazellier and Vassilicos [35] wake interaction length could collapse the behaviour of the fractal fences with some success in this region.

In general, when more subtle properties of the flow field are studied, there are significant differences that are clearly expressed throughout the domain. The fractal fences induce a flow with a lower average (but more constant) Hölder exponent, meaning that intermittency is reduced but that the turbulence signal fluctuates to a greater extent. This reduction in intermittency seen in the Hölder exponents is also evident in the structure functions, which are closer to those predicted for isotropic turbulence. Indeed, we also find energy spectra that are closer to those for isotropic flow. Thus, a fractal forcing, because it promotes eddy interaction at a range of scales, reduces the coherence of large-scale structures for $x/H > 5.0$. This reduced intermittency has implications for sedimentation behind such fences. If the inertial scale of the particles is such that the small-scale structures seen in Fig. 11 are irrelevant for sedimentation, then deposition should be more efficient than for non-fractal fences where large-scale fluctuations (Fig. 10) mean that the inertia of individual flow structures is large enough to overcome particle scales. Conversely, for smaller particles with shorter inertial times, fractal fences are expected to be less efficient as the high frequency variations that these wakes exhibit will affect particle deposition.

The enhanced dissipation that we see in Figs. 14 and 15 is consistent with work using numerical fractal forcings, studied in the fluid mechanics literature, although the proportion of dissipation observed here in what notionally looks to be the “inertial regime” is less (although still double that for non-fractal fences). The manner in which energy transfer takes place in the wakes of fractal and non-fractal forced flows is clearly different and is currently the focus of significant research efforts in fluid mechanics [50]. It would seem that the term “inertial regime” may be inappropriate to describe the region of power-law spectral decay in fractal-forced wakes, even though the structure functions for fractal-forced flow appear to be more similar to isotropic turbulence. This is because significant dissipation is taking place within this scaling region compared to the wakes from fences that are forced in a more traditional manner. Enhanced dissipation (Fig. 14) coupled to a reduced rate of energy decay over wavenumbers corresponding to the forced scales (Fig. 13) implies that turbulence production must be higher for the multi-scale forced flow and hints at the potential for optimising fence design to control for production or dissipation depending on the application.

The immediate conclusion from our work is that specifying a height, porosity and bottom gap size for a fence is not sufficient to determine the wake structure of turbulence: the arrangement of the fence struts also has an effect, although porosity effects clearly dominate the primary turbulence variables such as the mean flow and turbulence intensity. More generally, the high dissipation that was seen to occur in a realm that looked like an inertial regime may be a property of many other types of environmental boundary-layer flows owing to the complexity of the forcing that often occurs, such as flows through a forest forced at scales from leaf to trunk Finnigan [12]. This property of environmentally forced turbulence means that it is debateable if an “inertial regime” *sensu strictu* exists in multi-scale forced flows, and this and other conclusions from the emerging literature on fractal and broadband forcing are deserving of greater attention.

Acknowledgments We are grateful to the workshop at the Institute of Low Temperature Science, University of Hokkaido who constructed the fences used in these experiments. This research was undertaken while CK was in receipt of a short-term fellowship from the Japan Society for the Promotion of Science (PE 04511) hosted by the Nagaoka Institute for Snow and Ice Studies.

References

1. Anselmet F, Gagne Y, Hopfinger E, Antonia RA (1984) High-order velocity structure functions in turbulent shear flow. *J Fluid Mech* 140:63–89
2. Babiano A, Dubrulle B, Frick P (1995) Scaling properties of numerical 2-dimensional turbulence. *Phys Rev E* 52:3719–3729
3. Batchelor GK (1953) *The theory of homogeneous turbulence*. Cambridge University Press, Cambridge
4. Benzi R, Ciliberto S, Tripiccion R (1993) Extended self-similarity in turbulent flows. *Phys Rev E* 48:R29–R32
5. Benzi R, Ciliberto S, Baudet C, Chavarría GR (1995) On the scaling of 3-dimensional homogeneous and isotropic turbulence. *Physica D* 80:385–398
6. Chaudhary V, Mathur P (2004) Composite avalanche control scheme developed for the lower himalayan zone: a case history. *Cold Reg Sci Technol* 39:243–255
7. Chen SY, Dhruva B et al (2005) Anomalous scaling of low-order structure functions of turbulent velocity. *J Fluid Mech* 533:183–192
8. Cheskidov A, Doering CR, Petrov N (2007) Energy dissipation in fractal-forced flow. *J Math Phys* 48:065,208
9. Comte-Bellot G, Corrsin S (1966) The use of a contraction to improve the isotropy of grid-generated turbulence. *J Fluid Mech* 25:657
10. Dong ZB, Chen GT, He XD (2004) Controlling blown sand along the highway crossing the taklimakan desert. *J Arid Environ* 57:329–344
11. Donoho DL, Johnstone I (1994) Ideal spatial adaptation by wavelet shrinkage. *Biometrika* 81:425–455
12. Finnigan J (2000) Turbulence in plant canopies. *Ann Rev Fluid Mech* 32:519–571
13. Frisch U, Parisi G (1985) The singularity structure of fully developed turbulence. In: Ghil M, Benzi R, Parisi G (eds) *Turbulence and predictability in geophysical fluid dynamics and climate dynamics*. North-Holland, Amsterdam, pp 84–88
14. Gaudin E, Protas B, Goujon-Durand S, Wojciechowski J, Wesfriedl JE (1998) Spatial properties of velocity structure functions in turbulent wake flows. *Phys Rev E* 57:R9–R12
15. George WK (1992) The decay of homogeneous isotropic turbulence. *Phys Fluids A* 4:1492
16. George WK, Wang H (2009) The exponential decay of homogeneous isotropic turbulence. *Phys Fluids* 21:108
17. Gledzer E (1997) On the Taylor hypothesis corrections for measured energy spectra of turbulence. *Physica D* 104:163–183
18. Goring DG, Nikora VI (2002) Despiking acoustic doppler velocimeter records. *ASCE J Hydraul Eng* 128:117–126
19. Hurst D, Vassilicos JC (2007) Scalings and decay of fractal-generated turbulence. *Phys Fluids* 19:103
20. Iversen JD (1984) Comparison of snowdrift modeling criteria—commentary on application of anno modeling conditions to outdoor modeling of snowdrifts. *Cold Reg Sci Technol* 9:259–265
21. Keylock CJ (2006) Constrained surrogate time series with preservation of the mean and variance structure. *Phys Rev E* 73:036,707
22. Keylock CJ (2007) The visualisation of turbulence data using a wavelet-based method. *Earth Surf Proc Land* 32:637–647
23. Keylock CJ (2008) A criterion for delimiting active periods within turbulent flows. *Geophys Res Lett* 35:L11,804
24. Keylock CJ (2009) Evaluating the dimensionality and significance of “active periods” in turbulent environmental flows defined using Lipschitz/Hölder regularity. *Environ Fluid Mech* 9:509–523
25. Keylock CJ (2010) Characterizing the structure of nonlinear systems using gradual wavelet reconstruction. *Nonlin Proc Geophys* 17:615–632
26. Kolmogorov AN (1941) The local structure of turbulence in incompressible viscous fluid for very large Reynolds numbers. *Dokl Akad Nauk SSSR* 30:299–303
27. Kolmogorov AN (1962) A refinement of previous hypotheses concerning the local structure of turbulence in a viscous, incompressible fluid at high Reynolds number. *J Fluid Mech* 13:82–85
28. Kolwankar KM, Lévy Véhel J (2002) A time domain characterisation of the fine local regularity of functions. *J Fourier Anal Appl* 8:319–334
29. Kosugi K, Sato T, Sato A (2004) Dependence of drifting snow saltation lengths on snow surface hardness. *Cold Reg Sci Technol* 39:133–139
30. Kuczaj AK, Geurts BJ (2006) Mixing in manipulated turbulence. *J Turbul* 7:1–28
31. Kuczaj AK, Geurts BJ, McComb WD (2006) Nonlocal modulation of the energy cascade in broadband-forced turbulence. *Phys Rev E* 74:016,306

32. Laizet S, Vassilicos JC. Dns of fractal-generated turbulence. *Flow Turbulence Combust* doi:[10.1007/s10494-011-9351-2](https://doi.org/10.1007/s10494-011-9351-2)
33. Lang RM, Blaisdall GL (1998) Passive snow removal with a vortex generator at the pegasus runway, antarctica. *Ann Glaciol* 26:231–236
34. Lumley JL (1965) Interpretation of time spectra measured in high intensity shear flows. *Phys Fluids* 8:1056–1062
35. Mazellier N, Vassilicos JC (2010) Turbulence without Richardson–Kolmogorov cascade. *Phys Fluids* 22:075,101
36. Mazzi B, Vassilicos JC (2004) Fractal-generated turbulence. *J Fluid Mech* 502:65–87
37. Mazzi B, Okkels F, Vassilicos JC (2002) A shell-model approach to fractal-induced turbulence. *Eur Phys J B* 28:243–251
38. McCoy A, Constantinescu G, Weber L (2007) A numerical investigation of coherent structures and mass exchange processes in channel flow with two lateral submerged groynes. *Water Resour Res* 43:W05,445. doi:[10.1029/2006WR005267](https://doi.org/10.1029/2006WR005267)
39. Meneveau C, Sreenivasan KR (1987) Simple multifractal cascade model for fully developed turbulence. *Phys Rev Lett* 59:1424–1427
40. Muzy JF, Bacry E, Arnéodo A (1991) Wavelets and multifractal formalism for singular signals: Application to turbulence data. *Phys Rev Lett* 67:3515–3518
41. Naaim-Bouvet F, Naaim M, Michaux JL (2002) Snow fences on slopes at high wind speed: physical modelling in the cstb cold wind tunnel. *Nat Hazard Earth Syst* 2:137–145
42. Nemoto M, Nishimura K (2001) Direct measurement of shear stress during snow saltation. *Boundary-Layer Meteorol* 100:149–170
43. Nemoto M, Nishimura K (2004) Numerical simulation of snow saltation and suspension in a turbulent boundary layer. *J Geophys Res* 109. doi:[10.1029/2004JD004657](https://doi.org/10.1029/2004JD004657)
44. Percival DB, Walden AT (2000) *Wavelet methods for times series analysis*. Cambridge University Press, Cambridge
45. Pinton JF, Labbé R (1994) Correction to the Taylor hypothesis in swirling flows. *J Phys II* 4:1461–1468
46. Saddoughi SG, Veeravali SV (1994) Local isotropy in turbulent boundary-layers at high Reynolds number. *J Fluid Mech* 268:333–372
47. Seoud RE, Vassilicos JC (2007) Dissipation and decay of fractal generated turbulence. *Phys Fluids* 19:108
48. She ZS, Leveque E (1994) Universal scaling laws in fully developed turbulence. *Phys Rev Lett* 72:336–339
49. Staicu A, Mazzi B, Vassilicos JC, van de Water W (2003) Turbulent wakes of fractal objects. *Phys Rev E* 67:066,306
50. Stresing R, Peinke J, Seoud S, Vassilicos JC (2010) Defining a new class of turbulent flows. *Phys Rev Lett* 104:194,501
51. Tabler RD (1980) Geometry and density of drifts formed by snow fences. *J Glaciol* 26:405–419
52. Tabler RD (1991) *Snow fence guide*. Strategic Highway Research Program SHRP-H-320. National Research Council, Washington
53. Takeuchi Y, Kobayashi S, Sato T (2001) The effect of wind direction on drift control by snow fences. *Ann Glaciol* 32:159–162
54. Vassilicos JC, Hunt JCR (1991) Fractal dimensions and spectra of interfaces with application to turbulence. *Proc R Soc Lond A* 435:505–534
55. von Karman T, Howarth L (1938) On the statistical theory of turbulence. *Proc R Soc Lond Ser A* 164:192
56. Wang H, George WK (2002) The integral scale in homogeneous, isotropic turbulence. *J Fluid Mech* 459:429